Journal of Power Sources 213 (2012) 287–295

Contents lists available at SciVerse ScienceDirect

Journal of Power Sources

journal homepage: www.elsevier.com/locate/jpowsour

Structural study of $LiFePO_4$–$LiNiPO_4$ solid solutions

Lubna Tabassam [a], Gabriele Giuli [a], Arianna Moretti [a], Francesco Nobili [a], Roberto Marassi [a], Marco Minicucci [a,b], Roberto Gunnella [a,b], Luca Olivi [c], Andrea Di Cicco [a,b,d,*]

[a] School of Science and Technology, University of Camerino, I-62032 Camerino, Italy
[b] CNISM, Consorzio Interuniversitario di Struttura della Materia, Sezione di Fisica, Università di Camerino, Italy
[c] Synchrotron ELETTRA, Strada Statale 14, I-34149 Basovizza, Trieste, Italy
[d] IMPMC, Université Paris 6, CNRS, Campus Jussieu, F-75005 Paris, France

ARTICLE INFO

Article history:
Received 27 January 2012
Received in revised form
14 April 2012
Accepted 17 April 2012
Available online 24 April 2012

Keywords:
Olivine $LiFePO_4$
Ni doping
Cyclic voltammetry
Rietveld
XANES
EXAFS

ABSTRACT

Modifications of the local structure and lattice parameters in $LiFe_{1-x}Ni_xPO_4$ ($0 < x < 0.15,0.9,1.0$) olivine-type solid solutions have been studied by X-ray diffraction (XRD) and X-ray absorption spectroscopy (XAS). Samples have been synthesized and characterized in our laboratory, and a preliminary electrochemical characterization shows that Ni doping increases slightly the performances in Li-ion cells at low Ni concentrations *x*. Results of both XRD and XAS techniques are consistent and indicate ordering of Li in the M1 site, and of Fe and Ni in the M2 site of the olivine structure. Ni doping is found to induce an anisotropic shrinking of the unit cell with both Fe and Ni six-coordinated with oxygens, occupying distorted octahedral sites. The local structure measured by XAS shows that average Fe–O and Ni–O distances do not change appreciably with Ni doping indicating that the reduction of cell size is mainly associated with the presence of shorter Ni–O distances at M2 sites. Possible connections among the presence of a distribution of distorted octahedra of different size in the structure and different electrochemical performances of the material as a function of doping are briefly discussed.

1. Introduction

In recent times, considerable efforts have been devoted to study physical and chemical properties of Li-phosphate olivines, mainly for their possible use as a storage cathode for rechargeable lithium batteries. Compounds under consideration include $LiMPO_4$ olivines where M is a transition metal (see for example [1]). Key factors for using these materials in batteries are their electrical and ion (Li^+) conductivities.

In particular, the olivine-type $LiFePO_4$ (triphylite) has attracted much attention as a suitable cathode material for high-power Li-based batteries [2]. $LiFePO_4$ has been extensively studied because of its attractive properties such as inexpensiveness, non-toxicity, high theoretical capacity (~ 170 mAh g^{-1}), excellent cycling and thermal stability [3–5].

The key drawbacks of $LiFePO_4$ are its low electronic conductivity and reversible capacity. Various synthesis and processing approaches have been employed to improve the conductivity and cyclability of the $LiFePO_4$ [6–8]. Many studies have been devoted to optimize the material for better electrochemical performance and try to understand the lithium intercalation/deintercalation mechanism [9–11].

It has been shown [1,2] that significant increases of the electrical conductivity can be induced by controlled nonstoichiometry and cation doping, improving the performances of current electrodes.

Structural changes in triphylite due to solid solutions of a metal M with iron ($LiFe_{1-x}M_xPO_4$) may have significant effects on its solid electrolyte properties, including rates of Li diffusion and activation energies. Thus, detailed knowledge of structure in solid solutions is important in the development and design of Li-based olivine storage cathodes. Several structural studies have been performed on $LiFe_{1-x}M_xPO_4$ solid solutions [12–18], few discussing structural variations that occur as a function of M content *x*. In particular, no detailed structural works on $LiFe_{1-x}Ni_xPO_4$ solid solutions have been attempted so far, although this material can be possibly useful in a wide range of concentrations in view of the similarity of the cation radii.

In this work, we present new results of a structural study of $LiFe_{1-x}Ni_xPO_4$ solid solutions for different Ni concentration *x*.

* Corresponding author. School of Science and Technology, University of Camerino, I-62032 Camerino, Italy. Tel.: +39 3204381009; fax: +39 (0) 737402853.
E-mail addresses: lubnatabassam@gmail.com (L. Tabassam), andrea.dicicco@unicam.it (A. Di Cicco).

0378-7753/$ – see front matter © 2012 Elsevier B.V. All rights reserved.
doi:10.1016/j.jpowsour.2012.04.036

Synthetic materials, produced and characterized by us, have been studied by a combination of advanced techniques like X-ray Absorption spectroscopy (XAS) and X-ray diffraction (XRD). XRD Rietveld refinement is used to study variations of the lattice parameters and atomic fractional coordinates with concentration *x*, while XAS is used to provide information about local electronic and structural properties at cation sites (see for example [19–24] and refs. therein). The final aim of this work is to provide the basic knowledge of the structure, including local ordering and distortions at metal sites, for better understanding possible modifications induced in electrochemical performances in Li-ion batteries.

The structure of the paper is as follows: methods and results for synthesis and electrochemical characterization are reported in Sec. 2; X-ray diffraction structural refinements are presented and discussed in Sec. 3; data-analysis and results of both near-edge and extended X-ray absorption spectroscopy data are discussed in Sec. 4; conclusions and perspectives are briefly resumed in Sec. 5.

2. Synthesis and electrochemical characterization

Pristine ($LiFePO_4$) and Ni-doped ($LiFe_{(1-x)}Ni_xPO_4$) lithium iron phosphate powders were synthesized by solution deposition followed by calcination in reducing atmosphere [25]. $LiNO_3$ (Sigma–Aldrich, >99%), $Fe(NO_3)_3{\cdot}9H_2O$ (Sigma–Aldrich, >98%), $Ni(NO_3)_2$ and $NH_4H_2PO_4$ (Sigma–Aldrich, >99%) were used as precursors, while D(+)-Glucose (Sigma–Aldrich, ACS Reagent) was added as carbon source. Molar ratios between cations precursors have been tuned according to the desired stoichiometries. Precursors were dissolved in water under stirring for almost 1 h and then heated at 60–70 °C using a water bath. The resulting solid precursor was ground to a fine powder using a mortar, calcined at 350 °C for 4 h and finally sintered at 750 °C for 8 h. During synthesis, glucose converts to carbon to assist reduction of Fe(III) to Fe(II) and to produce a carbon coating of the $LiFe_{1-x}Ni_xPO_4$ powders. Glucose, and a 5% H_2/Ar atmosphere (P:C molar ratio 1:4), have been used to ensure reducing conditions suitable to the synthesis of the $LiFePO_4$ and $LiFe_{1-x}Ni_xPO_4$ powders at higher Fe contents (*x* between 0 and 0.15). In order to prevent phosphate reduction to inactive phosphides, $LiFe_{1-x}Ni_xPO_4$ compounds with lower Fe contents ($x = 0.9, 1$) have been synthesized using a lower P:C molar 1:2 ratio and a pure Ar atmosphere. We could not obtain stable $LiFe_{1-x}Ni_xPO_4$ solid solutions for intermediate Fe contents using the above-mentioned synthesis method. Ni and Fe amounts in the final composite powders have been estimated by ICP-OES elemental analysis, giving Ni/Ni + Fe ratios in good agreement with the expected stoichiometries. The amounts of carbon coating the grains of $LiFePO_4$ and $LiFe_{1-x}Ni_xPO_4$ powders have been estimated by elemental analysis, giving C contents between 5 and 10% weight overall.

As the Ni-doped samples are thought to be interesting materials for electrodes in batteries, we also performed an electrochemical characterization of some of the synthesized powders, namely pure $LiFePO_4$ and 3% Ni-doped $LiFe_{0.97}Ni_{0.03}PO_4$, in order to evaluate the effect of the doping. The electrodes have been manufactured by preparing a slurry of the active $LiFePO_4$ or $LiFe_{1-x}Ni_xPO_4$ materials, conductive carbon (Super P by MMM-carbon) and binder (polyvinylidene difluoride, PVDF by Sigma–Aldrich) in the mass ratio 80:10:10 in NM2P (N-methyl-2-pyrrolidinone). The resulting slurry was stirred for 4 h, treated in ultrasonic bath for 15 min and then coated on Al foil current collector using the "doctor blade" technique. The coating was dried in open air at 70 °C, then circular electrodes were cut (diameter = 9 mm), resulting in active mass loadings between 3 and 4 mg cm^{-2}. The cathodes were then dried under vacuum at 120 °C and finally brought inside a glove-box (O_2 and H_2O level below 10 ppm) for the assembling of T-shaped polypropylene Swagelok-type 3-electrode cells, equipped with stainless steel (SS304) rods as current collectors. A polypropylene film (Celgard 2400, Celanese Co.) was used as separator, while the electrolyte was 1 M $LiPF_6$ in EC:DMC 1:1 (LP30 by Merck). High purity Li (Aldrich) was used to prepare counter and reference electrodes. The electrochemical measurements have been performed by using a VMP2/Z multi-channel electrochemical workstation (Bio-Logic SaS, France). Cyclic voltammetries were performed at very slow scan rate (50 μV s^{-1}) between 2 and 4.2 V. Galvanostatic cyclations were run in the same potential range, at variable charge/discharge rates between C/10 and 5C (1C = 170 mA g^{-1}). All the measurements have been performed at $T = 20$ °C. All the potentials are given vs. Li^+/Li redox couple. For sake of comparison, all the values of current and capacity have been normalized to the active masses of the electrodes.

A preliminary characterization of the electrochemical behavior of one of the doped powders, namely the 3% Ni-doped $LiFePO_4$, has been carried out by cyclic voltammetry and galvanostatic cyclations at $T = 20$ °C, and compared with the behavior of the pristine $LiFePO_4$, in order to verify the effectiveness of the synthesized powders as cathode materials. Very slow cyclic voltammetries (scan rate = 50 μV s^{-1}) of both undoped and doped $LiFePO_4$ ($x = 0.03$) cathodes are shown in Fig. 1. Both electrodes exhibit two sharp, well defined peaks during oxidation and reduction. This shows that, for both undoped and doped samples, the charge/discharge processes mainly occur through a two-phase reaction between $LiFe_{1-x}Ni_xPO_4$ and $Fe_{1-x}Ni_xPO_4$. The midpoint potentials between the anodic and cathodic peaks are practically invariant for the two electrodes under investigation (3.423 V and 3.427 V for $x = 0$ and $x = 0.03$ doped compounds, respectively), showing that Ni doping does not affect sensibly the charge/discharge thermodynamics. At the same time, the separation between anodic and cathodic peaks is slightly reduced (115 mV for the undoped electrode, 105 mV for the doped one), revealing that Ni doping may play a role in a minor reduction of the electrode polarization. The amount of Li exchanged, as calculated from integration of oxidation currents, is slightly higher for the doped electrode as compared with the undoped one (135 instead of 125 mAh g^{-1}), suggesting

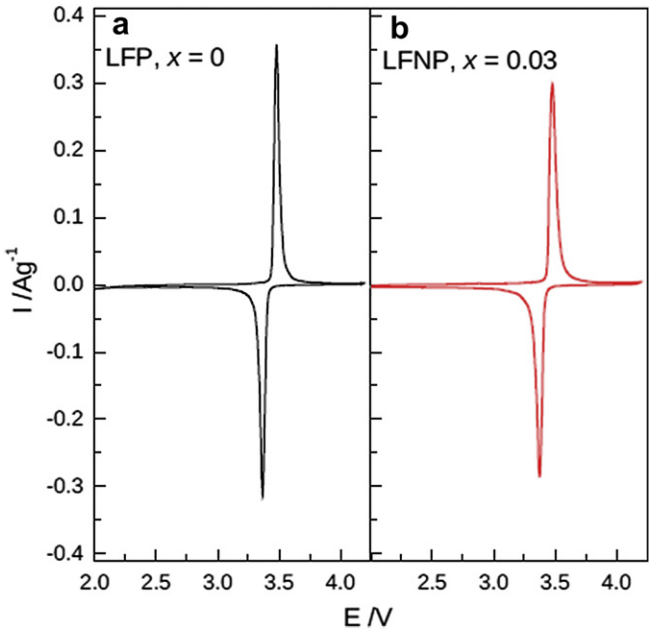

Fig. 1. Cyclic voltammetry of pristine $LiFePO_4$ (a) and $LiFe_{0.97}Ni_{0.03}PO_4$ (b). The scan rate was 50 μV s^{-1} at a temperature $T = 20$ °C.

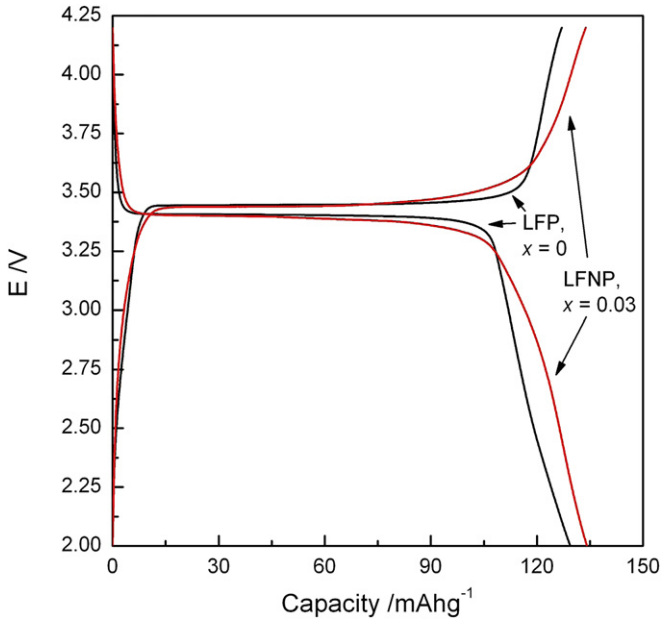

Fig. 2. Galvanostatic profiles of pristine $LiFePO_4$ and Ni-doped $LiFe_{0.97}Ni_{0.03}PO_4$ (charge/discharge rate = C/10, temperature $T = 20$ °C).

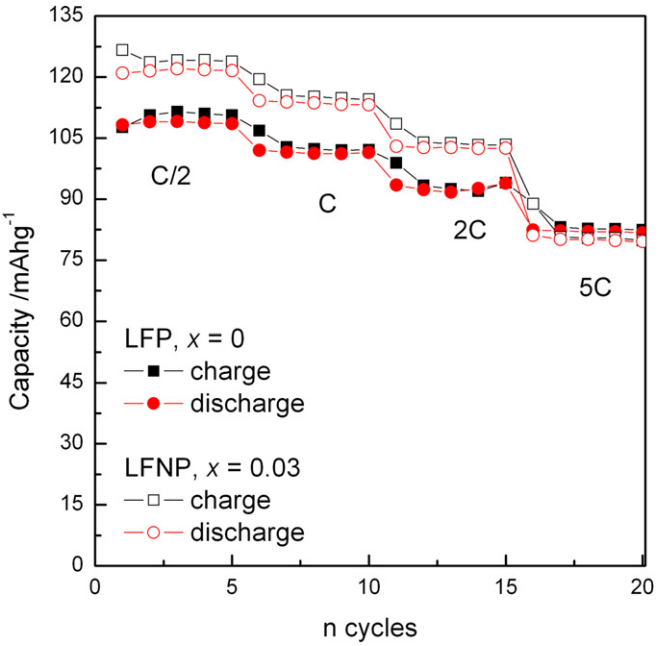

Fig. 3. Intercalation/deintercalation performances of pristine $LiFePO_4$ and Ni-doped $LiFe_{0.97}Ni_{0.03}PO_4$ for different charge/discharge rates ($T = 20$ °C).

that the reduction of polarization may produce a slight improvement in performances as well. This behavior is confirmed by the galvanostatic profiles E v. Q shown in Fig. 2. The galvanostatic cyclations have been performed at C/10, so that the potential vs. capacity profiles reflect quasi-equilibrium conditions. In these experimental conditions, the doped electrode $LiFe_{1-x}Ni_xPO_4$ ($x = 0.03$) delivers a capacity that is 5 mAh g^{-1} higher than the undoped one. This minor capacity improvement may be related with the slightly lower polarization of the $LiFe_{1-x}Ni_xPO_4$ ($x = 0.03$) electrode, that allows the cell to exchange higher amounts of Li^+ before the cut-off potential limits are reached and the charge/discharge processes are interrupted. Even if the differences in terms of reversible capacity are very limited, some changes in charge/discharge behavior can be however noticed. The different relative lengths of the plateaus and of the sloping lines exhibited by the galvanostatic profiles of the two electrodes suggest that Ni doping can play a role in modifying the mechanism of both two-phase transformation and solid solution formation processes. In fact, the plateaus corresponding to the two-phase region are wider for the undoped electrode, while departures from the plateau behavior, typical of a solid solution, are more pronounced for the Ni-doped cathode. This behavior can be tentatively explained by hypothesizing that possible distortions of local and average geometry of $LiFePO_4$ structure, induced by Ni doping, may alter the heterosite/triphylite interphase strains and the solid-state diffusivity of Li^+ ions, that concur in determining the insertion/deinsertion mechanisms [26].

Cycling performances have been characterized at several higher charge/discharge rates in the range C/2 to 5C. The results are shown in Fig. 3. Both electrodes show quite good capacity retention when the cycling rate is increased. In all the investigated conditions, it is confirmed that Ni doping can enhance charge/discharge performances. In addition, the differences between the performances of the doped cathode and the undoped one are reduced as the cycling rate is increased. This behavior can be explained by considering that for the Ni-doped electrode the solid-solution region exchanges more capacity than for the undoped one, as confirmed by the longer sloping line in the E vs. Q graphs in Fig. 2. The two-phase plateau commonly lies at potentials far from both the upper and the lower cut-off potentials, while the solid-solution regions, having pronounced E vs. Q slopes, intercept both potential limits, so that their extents are more affected by Ohmic polarization. As a consequence, when the charge/discharge rate is increased from C/2 to 5C, the cell polarization progressively hinders exchange of charge in the solid-solution sloping regions, interrupting the charge/discharge processes when the upper and lower potential cut-offs are met. As a final result, the gap between performances of the two electrodes is progressively reduced, and eventually canceled at 5C rate. Nevertheless, the higher capacities obtained up to 2C rate confirm that the Ni doping can positively affect the charge/discharge performances of $LiFePO_4$ cathode, by inducing structural modifications that modify the insertion/deinsertion mechanisms. Further studies are needed to determine relevant parameters related to transport properties, as ionic and electronic conductivity, while the support of in-situ structural determinations would be useful to clarify and validate the correlation between structural properties and phase transformation kinetics and thermodynamics. The results here presented, even if incomplete, are however consistent in showing a charge/discharge performances improvement by Ni doping, and encourage us in further investigating Ni-doped $LiFePO_4$ structures.

3. X-ray diffraction

Step scan X-ray diffraction (XRD) data were recorded using an automated PHILIPS diffractometer equipped with Soller slits, 1° divergence-slits, 0.1 mm receiving slits and a graphite diffracted-beam monochromator. The Cu X-ray tube was operated at 40 kV and 25 mA. The spectra were recorded in the 2θ range from 15° to 140° with a 0.02° step and 9 s counting time. The samples were prepared by lateral loading a brass sample holder in order to minimize possible preferential orientation of the powders.

Since the synthesis products were micro-crystalline powders, structural characterization was done by X-ray powder diffraction. The structure was refined with the program GSAS [27]. The peak shape was modeled with a pseudo-Voigt function. The FWHM (Full

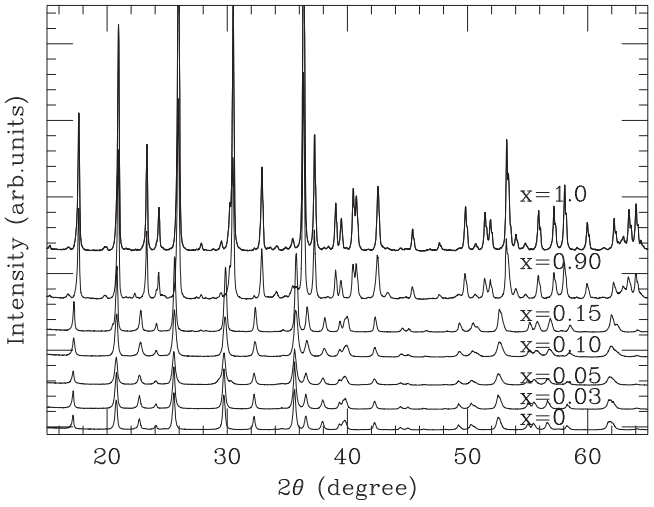

Fig. 4. X-ray diffraction patterns of the $LiFe_{1-x}Ni_xPO_4$ solid solutions obtained in this work for different doping fractions *x*.

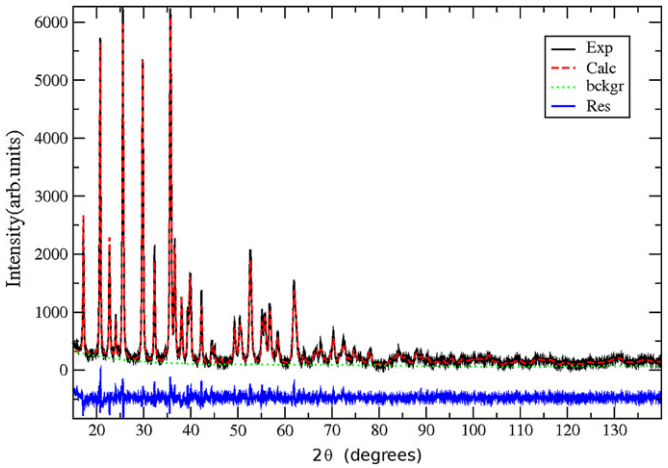

Fig. 5. Example of an XRD Rietveld refinement of the powder XRD pattern in the whole angular range ($LiFe_{1-x}Ni_xPO_4$, $x = 0.1$). Several curves are shown: experimental data (Exp, solid line), calculated pattern (Calc, dashed line), background (back, dotted), and residual curve (solid line, below).

Width Half Maximum) was refined as a function of the angle 2θ, taking into account both Gaussian and Lorentzian broadening. The refinement was carried out in the space group Pbnm. Starting atomic coordinates of $LiFePO_4$ were taken from Streltsov et al. [28]. Initial values of isotropic temperature factors were arbitrarily chosen as 0.025 $Å^2$ for all atoms. Cell parameters, scale factor and background polynomial function were left as free variables throughout the whole refinement. Refined parameters were included in this order: 2θ zero-shift, peak shape, sample displacement, atomic positional parameters, site occupancies, isotropic temperature factors. The intensity cut-off for the calculation of the profile step intensity was initially set at 1.0% of the peak maximum and, in the final stages of the refinement, was lowered to 0.1% of the peak maximum. Final convergence was assumed to be reached when the parameters shifts were <1% of their respective estimated standard deviation. Estimated errors provided by the Rietveld refinement program are ~0.0002 Å for the cell parameters and ~0.002 Å for the selected interatomic distances. However, the error calculation is probably over-optimistic as it does not include correlation among parameters and other source of errors (like the overlapping of many diffraction peaks). In order to get an alternative estimate of the accuracy of the refined structural data, we have compared the set of structural parameters obtained using different refinement strategies on the same diffraction data. These comparisons show that a realistic estimates of the error bars are ~0.001 Å for the cell parameters and ~0.007 Å for the selected interatomic distances. The latter values have been added as note to Table 1.

The XRD patterns of $LiFePO_4$ and Ni-doped $LiFePO_4$ are shown in Fig. 4. The sharp peaks indicate that the $LiFePO_4$ and Ni-doped $LiFePO_4$ samples are well crystalline. No carbon related peaks are detected, indicating that the residual carbon is XRD amorphous. Peak positions and intensities are clearly affected by Ni doping. With increasing Ni content *x*, peak positions systematically shift toward higher angles showing that the unit cell parameters decrease.

Li_3PO_4 and $Li_4P_2O_7$ are common impurities found in those materials. However, their concentration has always found to be small, and they do not affect the purity and electrochemical properties of the materials under investigation. Increasing Ni doping up to $x = 0.15$ showed no significant contents of impurity phases. However, significant amounts of Ni_3P have been found to occur at higher Ni contents ($x > 0.15$), thus limiting the possibility to obtain pure phases for such Ni concentrations. Materials at high Ni concentrations ($x = 1$ and $x = 0.9$) were successfully synthesized using a lower amount of carbon or without using H_2 in the oven in order to avoid formation of Ni_3P phosphides.

Rietveld refinement was used to obtain quantitative information about the crystal lattice structure. As an example, the observed, calculated and difference X-ray powder patterns of the synthetic $LiFe_{0.9}Ni_{0.1}PO_4$ sample are shown in Fig. 5. The results of the structural refinement, including the main structural parameters and disagreement indexes of the studied samples are summarized in Table 1.

It can be clearly seen that, upon Ni substitution, the unit cell parameters decrease (see Fig. 6). The unit cell volume decreases

Table 1
Results of the Rietveld refinement for $LiFe_{1-x}Ni_xPO_4$ samples with different concentration *x* obtained in this work: lattice parameters (a_0, b_0, c_0), unit cell volume, and average interatomic distances at the octahedral (M1, M2) and tetrahedral (T) sites. All distance and lattice parameters units are in Å (10^{-10} m). Volume unit is $Å^3$. Error bars on lattice parameters were found to be less than 0.001 Å while uncertainty on interatomic distances is estimated to be 0.007 Å (see text). Agreement indexes for the Rietveld refinement, as defined in ref. [27], are reported in the last three columns.

Sample: $LiFe_{(1-x)}Ni_xPO_4$										
x	a_0	b_0	c_0	Volume	⟨M1–O⟩	⟨M2–O⟩	⟨T–O⟩	R_{wp}	R_p	R_{F^2}
0.00	4.697	10.323	6.008	291.30	2.137	2.169	1.534	10.46	7.87	5.21
0.03	4.693	10.317	6.003	290.64	2.144	2.165	1.525	9.73	7.68	3.81
0.05	4.694	10.314	6.002	290.55	2.133	2.167	1.528	11.16	8.07	6.82
0.10	4.694	10.284	5.989	289.08	2.140	2.162	1.523	8.23	6.33	2.75
0.15	4.690	10.275	5.983	288.32	2.136	2.173	1.519	10.05	7.76	4.79
0.90	4.685	10.044	5.864	275.96	2.114	2.089	1.547	13.72	9.54	6.46
1.00	4.682	10.045	5.861	275.62	2.110	2.090	1.559	13.07	9.54	6.46

from 291.3 to 275.6 Å^3 (-5.4% of the initial volume) increasing the Ni concentration from $x = 0$ to $x = 1$. The unit cell volume contraction is markedly anisotropic: the b_0 parameter shows the most significant decrease, whereas the a_0 parameter decreases only slightly.

The structural refinements have been carried out assuming that the fractional occupancies of Ni at the octahedral M2 site are equal to the Ni fraction of the synthesized samples. Fractional occupancies have not been refined because of the similar X-ray scattering factors of Fe and Ni. Instead, several trials have been performed by refining the fractional occupancies of Fe or Ni at the M1 site in order to verify if Fe or Ni could substitute for Li. As the refined Fe or Ni occupancies at the M1 site were always lower than 0.02 for all the samples, we assumed that Li and Fe (or Ni) occupy only the M1 and M2 sites respectively.

Selected average nearest-neighbor interatomic distances, obtained by the Rietveld refinement, are reported in Table 1 and Fig. 7. The ⟨M−O⟩ (metal−oxygen) distances are reported in column 6 and 7 of Table 1 for the various materials with different Ni concentration x. The ⟨M2−O⟩ (Fe/Ni in a octahedral site) distance displays the strongest variation with a marked decrease from about 2.17 Å to 2.09 Å, as shown in Fig. 7. The ⟨M1−O⟩ distance displays a modest decrease from about 2.14 Å to 2.11 Å, whereas the average ⟨T−O⟩ distance shows a small increase from about 1.525 to 1.55 Å. The ⟨T−O⟩ distance variation, being smaller than 3 times the estimated uncertainty, cannot be considered significant. The fact that the strongest variation is observed for the ⟨M2−O⟩ distance is consistent with the occupation of the M2 site by Ni atoms. In fact, the decrease of the ⟨M2−O⟩ average distance reflects the smaller ionic radius of Ni^{2+} in octahedral coordination as compared to that of Fe^{2+} [29]. The overall decrease of the unit cell volume as a function of the Ni fraction can be thus ascribed to the decrease of the M2 average size with increasing Ni occupancy. Moreover, as the size and geometry of the M1 and the T site are also subject to minor variations to accommodate the varying geometrical shape of the M2 site, we observe also that the O1−O2−O1 angle decreases, determining a shortening of the M1 octahedral chain.

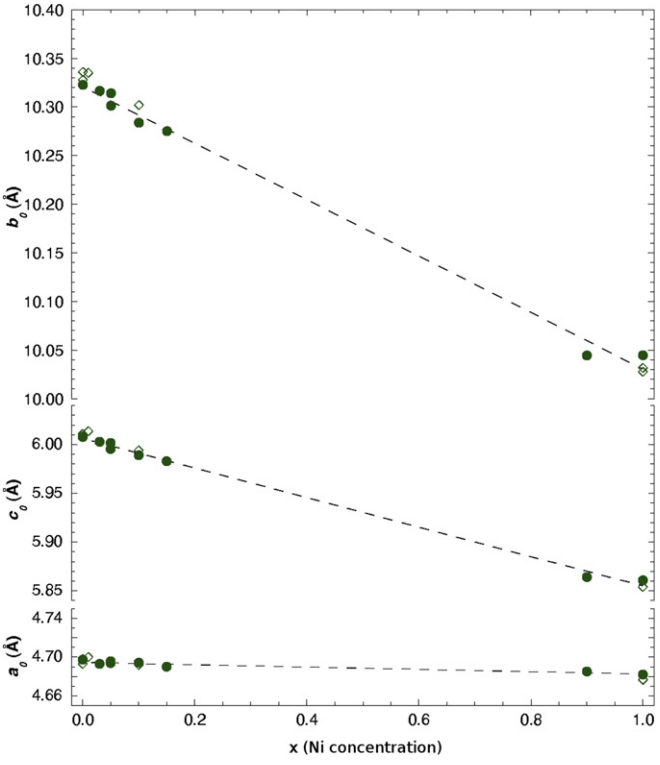

Fig. 6. Unit cell parameters a_0, b_0, and c_0 of $LiFe_{1-x}Ni_xPO_4$, as a function of Ni concentration x. Solid circles refer to the present study, whereas empty diamonds refer to literature data [13,14,30]. A simple linear fitting (dashed lines in the figure, parameters reported in Table 2) accounts for the contraction of the lattice parameters at increasing Ni doping.

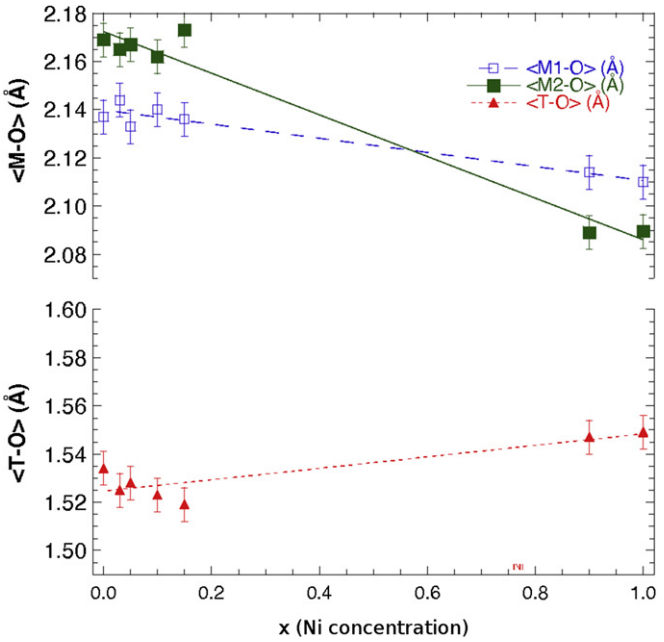

Fig. 7. Average first-neighbor interatomic distances as determined by XRD Rietveld refinement, for different Ni concentrations x. ⟨M−O⟩ (metal−oxygen) average distances are reported as squares (filled or empty for M2 and M1 sites respectively). ⟨T−O⟩ distances are reported as filled triangles in the lower part of the figure. Linear interpolations of those distances are shown as dashed lines.

The average ⟨M2−O⟩ interatomic distance, as measured by Rietveld analysis, was found to decrease significantly with Ni content x. The variation of ⟨M2−O⟩ distance is compatible with the different values of Fe and Ni covalent or ionic radii in octahedral coordination. On the other hand, the ⟨M1−O⟩ and ⟨T−O⟩ average distances were found respectively slightly decreasing or remain practically constant (within the estimated error bar) with Ni doping x.

As a result of the above-mentioned observations, we can ascribe the overall decrease of the unit cell volume with Ni content x to the decrease of the M2 average size of the distorted octahedra around Ni. The resulting structure of the solid solution can be thus viewed as a connected network of distorted M2 octahedra of different sizes (see also next Sec. 4).

Both the unit cell parameters and volume variations with x follow closely linear relationships (drawn also in Fig. 6 as dashed lines). Parameters of these linear refinements are reported in Table 2 with their estimated errors. The parameters of the linear relationships obtained in this study also represent a good fit to literature data [13,14,30] reported on Ni-doped $LiFePO_4$ samples.

4. X-ray absorption

X-ray Absorption Spectroscopy (XAS) measurements were performed at the Synchrotron Light Laboratory ELETTRA (XAFS station, Trieste, Italy) using a double-crystal monochromator equipped with Si(111) crystal [31] during dedicated beamtime. Fe K-edge and Ni K-edge XAS measurements were performed on $LiFe_{1-x}Ni_xPO_4$ samples at room temperature in transmission mode, using ionization chambers as photon counters (filled with appropriate Ar/He mixtures). Samples for XAS measurements in transmission mode

Table 2
Coefficients for the linear fit of the experimentally determined unit cell parameters and volume, in the form $y = \alpha + \beta^* x$, where x is the Ni concentration. Estimated statistical errors are shown in brackets.

$LiFe_{(1-x)}Ni_xPO_4$		
Unit cell par.	α	β
a_0	4.695 (1)	−0.012 (2)
b_0	10.321 (5)	−0.290 (9)
c_0	6.006 (2)	−0.1513 (4)
V_0	291.0 (2)	−16.0 (4)

were obtained by carefully mixing finely grounded specimen powders with graphite, producing pellets of appropriate thickness, chosen to give an optimal jump at the Fe and Ni absorption K-edges. High-quality spectra (S/N ratio higher than 10^4) were obtained even for the most diluted samples, increasing counting times up to about 20 s point^{-1}. Energy calibration was continuously monitored by simultaneous collection of XAS spectra of Fe and Ni metal foils using a third ionization chamber.

Experimental XANES (X-ray Absorption Near Edge Structure) spectra were reduced by background subtraction with a linear function and then normalized for atomic absorption to the average absorption coefficient of the spectral region from 7150 to 7300 eV. The threshold energy was taken as the first maximum of the first derivative of the spectra, whereas peak positions were obtained by calculating the second derivative of the spectra. Pre-edge peak analysis was carried out following the same procedures reported previously [19–21].

The pre-edge peak region was analyzed by first subtracting an arc-tangent background from the normalized spectra and then by fitting the pre-edge peak with a sum of pseudo-Voigt functions. Pre-edge peak intensities along with energy positions were compared with those of the standards analyzed here and others from the literature [19,20] in order to extract information on Fe oxidation state and coordination number in the glasses studied. Particular care was taken in using the smallest possible number of components in the pre-edge peak fitting procedure. In particular, the number and energy of the components was constrained to match those of the minima in the second derivative spectrum of the pre-edge peak. Several procedures have been tried for the pre-edge peak fitting: (1) simultaneous fitting of the background and the pseudo-Voigt component; (2) preliminary background subtraction followed by fitting with pseudo-Voigt components allowing the components to have different FWHM or Lorentian character; (3) preliminary background subtraction followed by fitting with pseudo-Voigt components constrained to have the same FWHM and Lorentian character. The third procedure (3) usually produces the best results in terms of scatter of pre-edge peak integrated intensity and centroid energy [32]. In particular, reproducibility of the integrated intensity has been estimated to be within ±0.01 by performing several fits to the background-subtracted pre-edge peaks. Use of different procedures for arc-tangent background subtraction, however, can lead to higher errors in the integrated intensity, up to ±0.035. The energy-intensity data of the fitted pre-edge peaks were compared with mixing lines calculated as intensity-weighted averages of two end-members: for divalent iron an ideal pre-edge peak has been chosen with integrated intensity equal to 0.074 (consistent with distorted octahedral Fe coordination) and an energy 0.9 eV above the edge energy of metallic iron; for trivalent iron an integrated intensity has been chosen as 0.104 (also consistent with distorted Fe^{+3} octahedral coordination) and an energy 2.4 eV above the edge energy of metallic iron. Normalized Fe K-edge XANES spectra of the studied samples are shown in Fig. 8 (left panel) arranged in order of increasing Ni content x from bottom to top. The general shape of these spectra is comparable to Fe K-edge XANES data of $LiFePO_4$ samples available in the literature [22–24].

Changes in the pre-edge peak (P) structure are known to be associated with variations of the Fe oxidation state and local structure. This peak P is due to an s–d like electronic transition. Despite it is dipole-forbidden, it becomes partially allowed by mixing of the d-states of the transition metal with the p-states of the surrounding oxygen atoms. This implies that the pre-edge peak energy position and intensity are greatly affected by the average Fe oxidation state and coordination geometry [19,33,34]. In particular, accurate evaluation of the pre-edge peak centroid energy and integrated intensity and comparison with those of Fe model compounds can provide quantitative information on both Fe oxidation state and coordination environment [19–21]. Its intensity will be minimal in case of regular octahedral symmetry (O_h) around the absorber, whereas it will reach its maximum in the case of tetrahedral coordination (T_d).

The background-subtracted pre-edge peaks are shown in Fig. 8 (right panel) along with the pseudo-Voigt components and their sums, whereas their centroid energies and integrated intensity are reported in Table 3. Each pre-edge peak has been fitted with two components whose energies (around 7112.5 and 7114.1 respectively) are fairly consistent with those of Fe model compounds. The relative importance of divalent or trivalent Fe causes an increase of the individual components resulting in an energy shift of the pre-edge peak centroid.

The integrated intensity of the pre-edge peaks vs. their centroid energies are plotted in Fig. 9 along with the data of Fe model compounds analyzed here and elsewhere [19–21]. For the sake of simplicity, only the relative energy is plotted (0 refers to the first maximum of the first derivative of metallic Fe spectrum) in order to avoid confusion when comparing data with literature data where a different edge energy value for metallic Fe has been chosen.

All divalent Fe model compounds are associated with pre-peak energies close to 0.9 eV above the metallic Fe edge, whereas trivalent Fe model correspond to energies close to 2.5 eV. For a given energy, the intensities of the model compounds pre-edge peaks vary according to the Fe coordination geometry (the shaded ellipses refer to the range of coordination numbers – [4], [5], and [6] – in Fe model compounds). In order to obtain quantitative data on Fe oxidation state and coordination number, mixing lines have been calculated between pre-edge peak intensity and energy values representative of possible Fe structural roles in these samples (see e.g. $[4]Fe^{2+}$, $[5]Fe^{2+}$, $[4]Fe^{3+}$, $[5]Fe^{3+}$, $[6]Fe^{3+}$). All the pre-edge peak data of the investigated $LiFe_{(1-x)}Ni_xPO_4$ materials are compatible with the presence of $[6]Fe^{2+}$ and $[6]Fe^{3+}$. In Fig. 9 we show mixing line (dotted) best matching the experimentally determined pre-edge peak data of the six samples examined in this work. Comparison of the experimentally determined pre-edge peak data with the mixing line obtained allowed to determine the $Fe^{3+}/(Fe^{3+} + Fe^{2+})$ ratio (listed in Table 3).

Extended X-ray absorption fine structure (EXAFS) data, at both Fe and Ni K-edge of the set of Ni-doped samples under consideration, have been analyzed in the framework of the GNXAS data-analysis method [35,36]. EXAFS data (Fe K-edge data shown in Fig. 10) contain several individual contributions associated with first (Fe–O, Ni–O), second (Fe/Ni–P) and more distant neighbors, characteristic of the Olivine structure (see for example ref. [24]). Here we report the results of the EXAFS data-analysis of the first-neighbor (oxygen) shell, to be compared with X-ray diffraction results reported in the previous section.

The local structure around the Fe (and Ni) site is that of a distorted octahedron, therefore first-neighbor distances are scattered

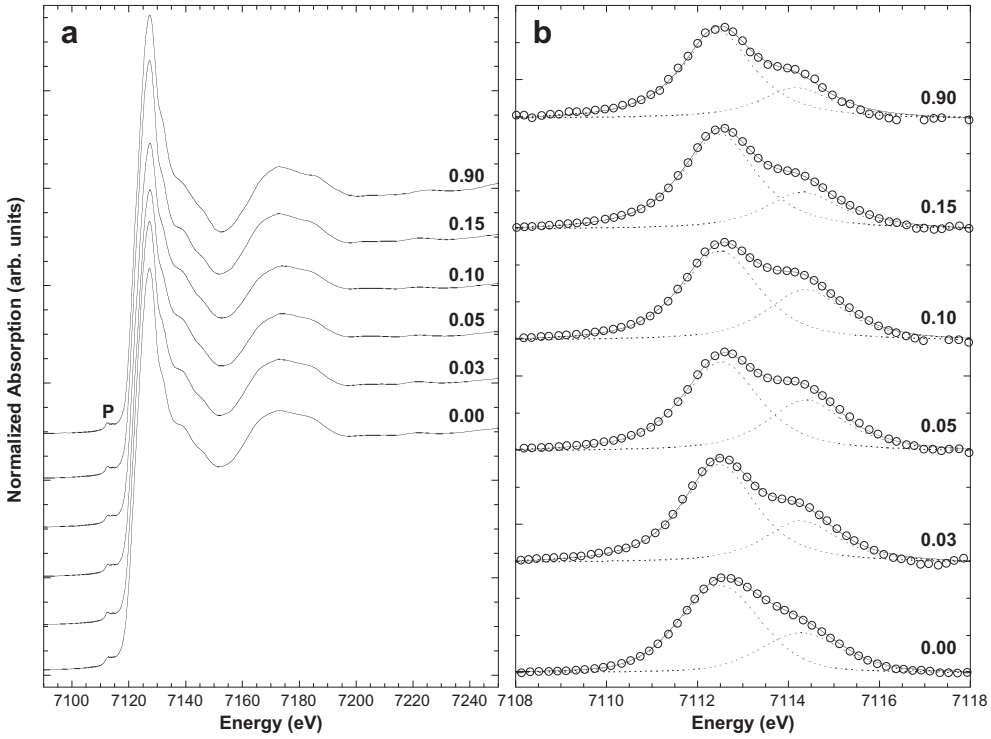

Fig. 8. Left panel: experimental normalized XANES spectra obtained at Fe K-edge of $LiFe_{1-x}Ni_xPO_4$ for increasing Ni concentration x from bottom ($x = 0$) to top ($x = 0.9$). Slight changes can be noted both in the pre-edge and near-edge regions. Right panel: background-subtracted pre-edge peaks of the studied samples (empty circles) along with the pseudo-Voigt components used in the fitting procedures (dotted lines), and their sums (solid lines). All curves (for increasing Ni concentration x) have been plotted with the same vertical scale in order to enable direct comparison of the intensities.

in a wide range (0.2 Å) around the typical Fe–O distance of about 2.1 Å. The average interatomic distance, as shown in Table 1, is a useful parameter for understanding changes occurring in the mean size of the octahedral site as a function of Ni doping. However, a more detailed model of the local structure is needed to reproduce the EXAFS spectra, which are sensitive to the first-neighbor bond distribution. We have verified that a single-shell model, including a single average Fe(Ni)–O distance and bond variance σ^2 is not able to account for the experimental EXAFS pattern. The best results are obtained using a multi-shell model, including shorter (~2.1 Å) and longer (~2.3 Å) Fe(Ni)–O bonds. Best-fit curves obtained using a simple two shell model with a minimal set of parameters, shown in Fig. 10 (dashed), are found to reproduce the first-neighbor component of the XAS spectra under consideration (for different Ni concentrations x). The model for local structure around Fe(Ni) includes 4 oxygen nearest neighbors and 2 more distant oxygens.

The EXAFS structural results are reported in Fig. 11 (squares, labeled as XAS) and compared with ⟨M–O⟩ distances obtained by XRD (circles, see also Table 1). As shown in Fig. 11 (upper panel) the

Table 3
Best-fit parameters for the pre-edge peak P (Fe K-edge) for different Ni concentrations x in the investigated samples. For each sample we report the centroid energy and the total intensity, as well as the parameters of the two individual pseudo-Voigt components. The agreement index (R) and the $Fe^{3+}/(Fe^{3+} + Fe^{2+})$ ratio (estimated error in brackets) are reported in the last two columns.

x	Peak component	Energy (eV)	Int. ty	FWHM (eV)	Area	Centroid	R (%)	Fe^{3+}/Fe^{tot}
0.0	Sum				0.085	7113.07	99.98	0.08 (5)
	1	7112.50	0.024	2.096	0.058			
	2	7114.27	0.011	2.096	0.027			
0.03	Sum				0.087	7112.99	99.82	0.04 (5)
	1	7112.48	0.027	1.915	0.062			
	2	7114.28	0.011	1.915	0.025			
0.05	Sum				0.089	7113.20	99.92	0.15 (5)
	1	7112.53	0.025	1.953	0.057			
	2	7114.38	0.013	1.953	0.032			
0.10	Sum				0.088	7113.17	99.89	0.13 (5)
	1	7112.50	0.025	2.020	0.057			
	2	7114.37	0.014	2.020	0.031			
0.15	Sum				0.082	7112.98	99.93	0.04 (5)
	1	7112.48	0.026	1.958	0.060			
	2	7114.31	0.010	1.958	0.022			
0.90	Sum				0.067	7112.85	99.93	0.00 (5)
	1	7112.45	0.024	1.879	0.051			
	2	7114.16	0.008	1.879	0.016			

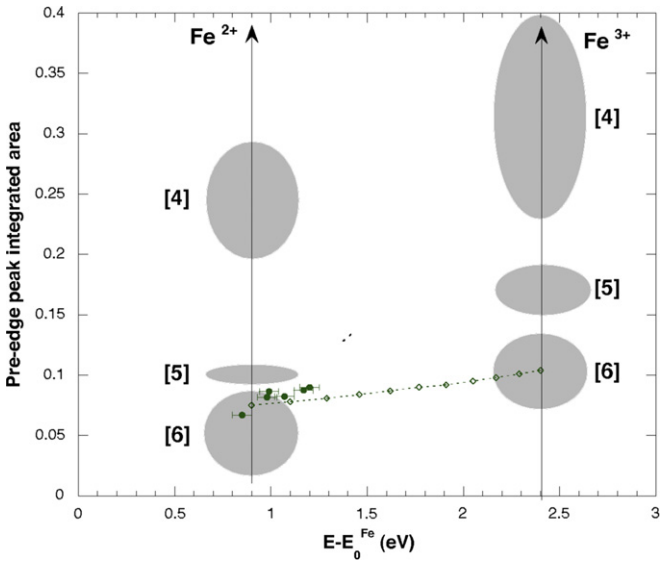

Fig. 9. Plot of the pre-edge peak integrated intensity vs. centroid energy position. Solid circles refer to the synthetic samples. The small empty circles joined by the dotted lines represent mixing lines calculated by linear combinations of [6]Fe^{2+} and [6]Fe^{3+} pre-edge peaks. The position of the experimentally measured pre-edge peaks with respect to the mixing line allows to determine quantitatively the $Fe^{3+}/(Fe^{2+}+Fe^{3+})$ ratio.

Fe—O and Ni—O bond distances are practically not influenced by doping within the estimated uncertainty (dashed and dotted lines). In particular, the average interatomic ⟨M—O⟩ distance calculated for the six nearest oxygens ($N = 6$) are practically constant, while Ni—O nearest-neighbor distances ($N = 4$) are shorter than the Fe—O ones so that the average size of the Fe/Ni octahedra decreases with increasing Ni doping. The large stability of the bonding distance with doping is not unexpected at all, as it is well-known that the first-neighbor distances are strongly driven by the chemistry of the bonds as shown by several previous EXAFS works (see for example [37] and ref. therein). The so-called Vegard's law (linear change with Ni concentration x) still holds when applied to the lattice parameters, though.

The results obtained about Fe—O and Ni—O distances show that the structure of this solid solution contains distorted octahedral

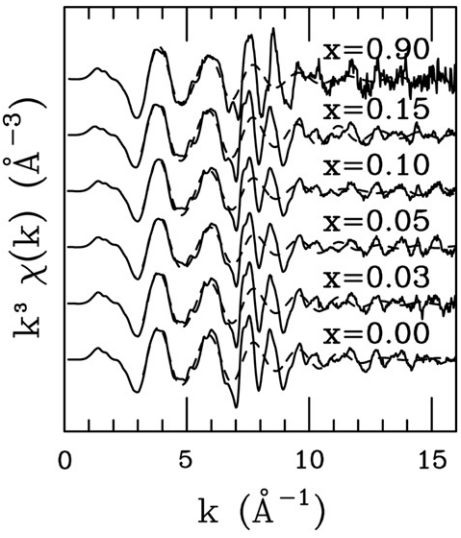

Fig. 10. Fe K-edge experimental (solid) and calculated (dashed) spectra of $LiFe_{1-x}Ni_xPO_4$ samples. Calculated signals include only the first-neighbor component.

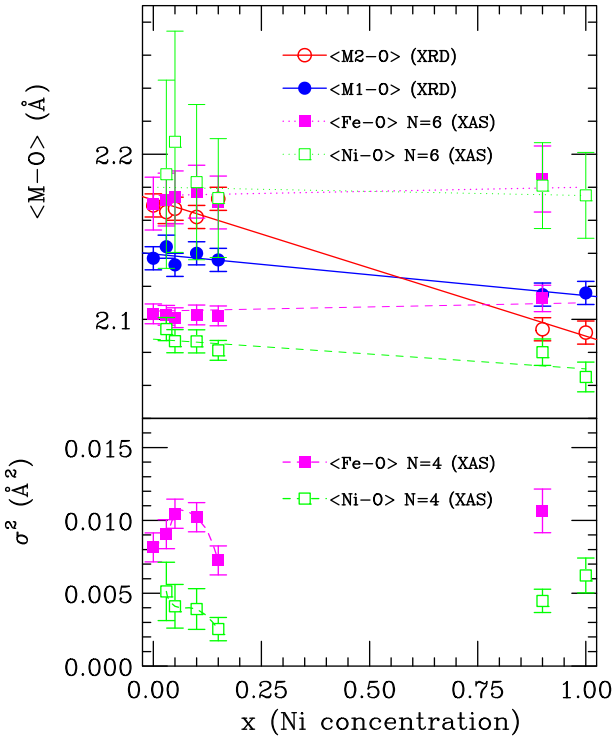

Fig. 11. Upper panel: comparison between first-neighbor metal-oxygen average distances obtained by XRD (circles, see Table 1) and XAS (squares) as function of Ni concentration x. XRD is associated with distances corresponding to distorted octahedral sites M1 and M2. XAS provides a direct local measurement of the average Fe—O (filled squares) and Ni—O (empty squares) bondlengths. We report both the average bond distances obtained by XAS for the nearest 4 oxygen neighbors ($N = 4$) and for all of the 6 oxygens ($N = 6$) of the distorted Fe—O or Ni—O octahedra. Lower panel: Fe—O (filled square) and Ni—O (empty squares) distance variances as determined by XAS for the first four nearest neighbors ($N = 4$).

structures of different size and geometry, depending whether they contain Fe or Ni, and therefore an augmented level of medium-range disorder is expected. The behavior of the σ^2 of the 4 shortest bondlengths Fe(Ni)—O, as a function of Ni concentration x, is reported in the lower panel of Fig. 11 and indicates that the level of structural disorder inside the distorted octahedral units does not change appreciably. The fluctuations of the Fe—O first-neighbor distances, including static and vibrational disorder, increase for low Ni concentrations x. It is interesting to remark that the Ni-based octahedral unit is strongly distorted with 4 bonds with distances in the 2.1 Å range, while the 2 longer bonds reach Ni—O distances around 2.4 Å. Both the spread of the Ni—O bondlengths and the different sizes of the Ni—O and Fe—O octahedra are expected to play a role in affecting the functional properties of these solid solutions. In fact, a strong interplay between the structure and the transport properties (ionic and electron) is expected. In particular, as discussed for example in refs. [38,39], topology and diffusion constants of the Li transport channels depend strongly on the structure. The presence of a distribution of distorted octahedra of different sizes in the olivine structure may induce changes in the electrochemical properties and in the intercalation/deintercalation kinetics, as a function of doping.

5. Conclusions

Samples of solid solutions $LiFe_{1-x}Ni_xPO_4$ with x ranging from 0.0 to 0.15 and from 0.9 to 1.0 were successfully synthesized and XRD Rietveld analysis shows that the unit cell volume decreases anisotropically with increasing Ni content x.

Results of both XRD and XAS techniques indicate that Li occupies the M1 site, while both Fe and Ni reside mostly in the M2 site of the olivine structure. The average ⟨M2–O⟩, ⟨M1–O⟩, and ⟨T–O⟩ equilibrium distances and the average Ni–O and Fe–O interatomic distances were obtained by XRD and XAS refinement respectively, showing that the overall linear decrease of the unit cell volume can be ascribed to the decrease of the M2 average size with increasing Ni occupancy. The shorter Ni–O bonding distances are found to induce a reduction of the average cell size, with an effect on the medium and long-range structure. Moreover, the Ni–O octahedral sites have been found to be largely distorted, with two atoms at longer distances.

It is encouraging that the comparison between the electrochemical properties of pristine and doped $LiFe_{1-x}Ni_xPO_4$ ($x = 0.03$) revealed both that our synthetic route can produce electroactive cathode materials, and that Ni doping can improve charge/discharge performances. This last feature is probably associated with a modification of the intercalation/deintercalation kinetics, possibly connected to the presence of a distribution of distorted octahedra of different sizes in the olivine structure as discussed above.

Further studies, focused both on the variation of the short and medium-range structure and on the electrochemical behavior of the $LiFe_{1-x}Ni_xPO_4$ system, are needed to validate the above-mentioned hypothesis and identify routes for improving electrode performances by modification and control of the microstructure.

Acknowledgments

Part of this work has been carried out using dedicated beamtime at the XAFS beamline at ELETTRA synchrotron (proj. 20110116), for which we acknowledge the scientific facility. We also thank E. Principi (University of Camerino/Sincrotrone Trieste) for his help in the very initial stage of the Ph.D. thesis project. L. T. gratefully acknowledges the University of Camerino for her Ph. D. grant.

References

[1] S.-Y. Chung, J.T. Bloking, Y.-M. Chiang, Nature Materials 1 (2002) 123–128.
[2] B. Kang, G. Ceder, Nature 458 (2009) 190–193.
[3] M. Armand, J.M. Tarascon, Nature 451 (2008) 652–657.
[4] J. Xu, G. Chen, Physica B: Condensed Matter 405 (2010) 803–807.
[5] N. Hua, C. Wang, X. Kang, T. Wumair, Y. Han, Journal of Alloys and Compounds 503 (2010) 204–208.
[6] H. Liu, C. Li, Q. Cao, Y.P. Wu, R. Holze, Journal of Solid State Electrochemistry 12 (2008) 1017–1020.
[7] J.W. Fergus, Journal of Power Sources 195 (2010) 939–954.
[8] I. Bilecka, A. Hintennach, M.D. Rossell, D. Xie, P. Novak, M. Niederberger, Journal of Materials Chemistry 21 (2011) 5881.
[9] C. Delmas, M. Maccario, L. Croguennec, F.L. Cras, F. Weill, Nature 7 (2008) 665–671.
[10] J. Hu, J. Xie, X. Zhao, H. Yu, X. Zhou, G. Cao, J. Tu, Journal of Materials Science and Technology 25 (2009) 405–409.
[11] Y. Lu, J. Shi, Z. Guo, Q. Tong, W. Huang, B. Li, Journal of Power Sources 194 (2009) 786–793.
[12] A. Losey, J. Rakovan, J.M. Hughes, C.A. Francis, M.D. Dyar, American Mineralogist 42 (2004) 1105–1115.
[13] P. Tang, N.A.W. Holzwarth, Physical Review B 68 (2003) 165107.
[14] D. Wang, H. Li, S. Shi, X. Huang, L. Chen, Electrochimica Acta 50 (2005) 2955–2958.
[15] C. Li, S. Zhang, F. Cheng, W. Ji, J. Chen, Nano Research 1 (2008) 242–248.
[16] H.C. Shin, S.B. Park, H. Jang, K.Y. Chung, W.I. Cho, C.S. Kim, B.W. Cho, Electrochimica Acta 53 (2008) 7946–7951.
[17] Y. Ge, X. Yan, J. Liu, X. Zhang, J. Wang, X. He, R. Wang, H. Xie, Electrochimica Acta 55 (2010) 5886–5890.
[18] W.-J. Zhang, Journal of Power Sources 196 (2011) 2962–2970.
[19] M. Wilke, F. Farges, P. Petit, G.E. Brown, F. Martin, American Mineralogist 86 (2001) 714–730.
[20] F. Farges, Physics and Chemistry of Minerals 28 (2001) 619–629.
[21] G. Giuli, G. Pratesi, E. Paris, C. Cipriani, Geochimica et Cosmochimica Acta 66 (2002) 4347–4353.
[22] A. Deb, U. Bergmann, E.J. Cairns, S.P. Cramer, The Journal of Physical Chemistry B 108 (2004) 7046–7051.
[23] A. Deb, U. Bergmann, E.J. Cairns, S.P. Cramer, Journal of Synchrotron Radiation 11 (2004) 497–504.
[24] M. Giorgetti, M. Berrettoni, S. Scaccia, S. Passerini, Inorganic Chemistry 45 (2006) 2750–2757.
[25] C.S. Sun, Z. Zhou, Z.G. Xu, D.G. Wand, J.P. Wei, X.K. Bian, J. Yan, Journal of Power Sources 193 (2009) 841–845.
[26] N. Meethong, H.-Y.S. Huang, W.C. Carter, Y.-M. Chiang, Electrochemical and Solid-State Letters 10 (2007) A134–A138.
[27] A. Larson, R.V. Dreele, in: General Structure Analysis System (GSAS), Los Alamos National Laboratory Report LAUR 86-748, 2004, pp. 1–224.
[28] V.A. Streltsov, E.L. Belokoneva, V.G. Tsirelson, N.K. Hansen, Acta Crystallographica Section B 49 (1993) 147–153.
[29] R.D. Shannon, Acta Crystallographica Section A 32 (1976) 751–767.
[30] W. Zhang, Y. Hua, X. Tao, H. Huang, Y. Gan, C. Wang, Journal of Physics and Chemistry of Solids 71 (2010) 1196–1200.
[31] A. Di Cicco, G. Aquilanti, M. Minicucci, E. Principi, N. Novello, A. Cognigni, L. Olivi, Journal of Physics: Conference Series 190 (2009) 012043.
[32] G. Giuli, E. Paris, K.U. Hess, D.B. Dingwell, M.R. Cicconi, S.G. Eckhout, K.T. Fehr, P. Valenti, American Mineralogist 96 (2011) 631–636.
[33] G. Calas, J. Petiau, Solid State Communications 48 (1983) 625–629.
[34] G.E. Brown, F. Farges, G. Calas, Reviews in Mineralogy, vol. 32, Mineralogical Society of America, Washington, D.C, 1995, pp. 317–410.
[35] A. Filipponi, A. Di Cicco, C.R. Natoli, Physical Review B 52 (1995) 15122–15134.
[36] A. Filipponi, A. Di Cicco, Physical Review B 52 (1995) 15135.
[37] A. Di Cicco, E. Principi, A. Filipponi, Physical Review B 65 (2002) 212106.
[38] D. Morgan, A.V. der Ven, G. Ceder, Electrochemical and Solid-State Letters 7 (2004) A30–A32.
[39] S.-i. Nishimura, G. Kobayashi, K. Ohoyama, R. Kanno, M. Yashima, A. Yamada, Nature Materials 7 (2008) 707–711.